

Unified Electronic Phase Diagram for Hole-Doped High- T_c Cuprates

T. Honma

*Department of Physics, Asahikawa Medical College, Asahikawa, Hokkaido 078-8510, Japan**

P. H. Hor

*Department of Physics and Texas Center for Superconductivity,
University of Houston, Houston, TX77204-5005, U.S.A.[†]*

(Dated: March 5, 2022)

We have analyzed various characteristic temperatures and energies of hole-doped high- T_c cuprates as a function of a dimensionless hole-doping concentration (p_u). Entirely based on the experimental grounds we construct a unified electronic phase diagram (UEPD), where three characteristic temperatures (T^* 's) and their corresponding energies (E^* 's) converge as p_u increases in the underdoped regime. T^* 's and E^* 's merge together with the T_c curve and $3.5k_B T_c$ curve at $p_u \sim 1.1$ in the overdoped regime, respectively. They finally go to zero at $p_u \sim 1.3$. The UEPD follows an asymmetric half-dome-shaped T_c curve in which T_c appears at $p_u \sim 0.4$, reaches a maximum at $p_u \sim 1$, and rapidly goes to zero at $p_u \sim 1.3$. The asymmetric half-dome-shaped T_c curve is at odds with the well-known symmetric superconducting dome for $\text{La}_{2-x}\text{Sr}_x\text{CuO}_4$ (SrD-La214), in which two characteristic temperatures and energies converge as p_u increases and merge together at $p_u \sim 1.6$, where T_c goes to zero. The UEPD clearly shows that pseudogap phase precedes and coexists with high temperature superconductivity in the underdoped and overdoped regimes, respectively. It is also clearly seen that the upper limit of high- T_c cuprate physics ends at a hole concentration that equals to 1.3 times the optimal doping concentration for almost all high- T_c cuprate materials, and 1.6 times the optimal doping concentration for the SrD-La214. Our analysis strongly suggests that pseudogap is a precursor of high- T_c superconductivity, the observed quantum critical point inside the superconducting dome may be related to the end point of UEPD, and the normal state of the underdoped and overdoped high temperature superconductors cannot be regarded as a conventional Fermi liquid phase.

PACS numbers: 74.25.Fy, 74.72.-h, 74.25.Dw

I. INTRODUCTION

The unique hallmark of high temperature superconductors (HTSs) is a pseudogap phase characterized by the observation of a multiple pseudogap temperatures (T^* 's) and pseudogap energies (E^* 's) by a large number of different experimental probes. While the pseudogap phase precedes the high temperature superconducting phase characterized by the superconducting transition temperature (T_c) and superconducting gap energy (Δ_c), it is not clear how T^* , T_c , E^* , and Δ_c are related to each other. Specifically, how are T^* and E^* related to the occurrence of the high- T_c superconductivity is still unclear. Is pseudogap a sufficient and/or necessary condition for high T_c or is it just a complication of specific material systems? Is it collaborating or competing with superconductivity? For instance, it is argued that the pseudogap is a competing order that may have nothing to do with high T_c .¹ On the other hand it is also suggested that the pseudogap is intimately related to high T_c .^{2,3} To distinguish these two contradictory pictures that are critical to the mechanism of high- T_c superconductivity requires a comparison of various characteristic temperatures and energies in a universal phase diagram for all HTSs. Any systematic behavior derived from this kind of phase diagram will provide true intrinsic properties of HTS that are free from material-specific complications. However, up until now there is no such a comparison made and no

such phase diagram available. We have analyzed numerous published data in the literature. We carefully select 27 HTSs: 11 single-layer, 11 double-layer and five triple-layer HTSs as summarized in the Table I. The selection criteria will follow when we discuss the construction of the figures. There are 15 different experimental probes used for these 27 HTSs which are summarized in Table II. In this paper we unify the characteristic temperatures of all these data of 27 HTSs on one single phase diagram entirely based on our proposed universal hole concentration scale that itself is also based on experimental results.

In the single-layer SrD-La214, where the hole-doping concentration can be unambiguously determined from the Sr-content (x),⁴ $T_c(x)$ exhibits a well-known symmetric bell-shaped curve, i.e., the so-called superconducting dome, with a maximum T_c (T_c^{max}) located at $x \sim 0.16$.⁵ The symmetrical dome-shaped T_c curve or the superconducting dome is approximately represented by the following parabola,

$$1 - \frac{T_c}{T_c^{max}} = 82.6 \times (x - 0.16)^2. \quad (1)$$

Assuming that all HTSs have the identical symmetric superconducting dome, x can be replaced with the hole-doping concentration (P_{T_c}). Then, this relation could be used to determine the hole-doping concentration for many other HTSs.^{5,6,7,8,9,10,11,12,13,14,15,16,17,18,19,20,21,22,23} Using

this hole-scale based on the superconducting dome, the P_{T_c} -scale, various phase diagrams have been constructed.¹ A distinct feature in one of such phase diagrams is that T^* crosses the superconducting dome and reaches zero at a quantum critical point (QCP) inside the dome.^{1,6} On the other hand, without using the P_{T_c} scale, some qualitative experimental observations seem to support another picture, where T^* touches the superconducting dome at around T_c^{max} and merges into the superconducting dome with no QCP inside the dome.² To distinguish these two fundamentally different pictures, we need a hole scale that can reveal the true intrinsic doping dependences of T^* , T_c , E^* , and Δ_c , which have been already observed.

The common structural features of HTS are CuO_2 -planes that host the doped holes and the block layers that supply the holes into the planes through oxygen-doping and/or cation-doping. While the doped hole-carriers

are initially confined in the CuO_2 -planes sandwiched between the insulator-like block layers, the holes are partially deconfined from the planes with doping. Therefore, the lightly doped HTS generally shows strongly two-dimensional (2D) properties. However, as the hole-doping increases, some physical properties are 2D and some, although built on the 2D carriers, will nominally be three-dimensional (3D) in nature. Therefore, it is necessary to use 2D and 3D carrier-doping concentrations to address 2D and 3D physical properties, respectively. To quantitatively study such dimensionality-dependent physical properties we have proposed a universal **planar** hole scale (P_{pl} -scale) for determining the hole-doping content per CuO_2 plane (P_{pl}).²⁴ In this scale, the P_{pl} is uniquely determined from S^{290} .²⁴ We showed that, in Ref. 24, the P_{pl} -scale is independent of the nature of the dopant, the number of CuO_2 -plane layers per formula unit cell (n_{layer}), the structure and the sample quality, namely, single crystal or not. This universal $S^{290}(P_{pl})$ -

TABLE I: The chemical formula and the notation for the HTSs used in the present work.

Chemical formula	Notation
(Single-layer HTS)	
$\text{La}_{2-x}\text{Sr}_x\text{CuO}_4$	SrD-La214
$\text{La}_{2-x}\text{Ba}_x\text{CuO}_4$	BaD-La214
La_2CuO_4	OD-La214
$(\text{Nd}_{1.6-x}\text{Ce}_x\text{Sr}_{0.4})\text{CuO}_4$	CeD-NdSr214
$(\text{La}_{1.6-x}\text{Nd}_{0.4}\text{Sr}_x)\text{CuO}_4$	SrD-LaNd214
$\text{Tl}_2\text{Ba}_2\text{CuO}_{6+\delta}$	OD-Tl2201
$\text{Bi}_2\text{Sr}_{2-x}\text{La}_x\text{CuO}_{6+\delta}$	CD-Bi2201
$(\text{Bi}_{1.74}\text{Pb}_{0.38})\text{Sr}_{1.88}\text{CuO}_{6+\delta}$	OD-BiPb2201
$(\text{Bi}_{1.35}\text{Pb}_{0.85})(\text{Sr}_{1.47-x}\text{La}_{0.38+x})\text{CuO}_{6+\delta}$	CD-BiPb2201
$\text{HgBa}_2\text{CuO}_{4+\delta}$	OD-Hg1201
$\text{Tl}_{1-x}\text{Pb}_x\text{Sr}_2\text{CuO}_{5-\delta}$	CD-TlPb1201
(Double-layer HTS)	
$\text{Y}_{1-x}\text{Ca}_x\text{Ba}_2\text{Cu}_3\text{O}_6$	CaD-Y1236
$\text{YBa}_2\text{Cu}_3\text{O}_{6+\delta}$	OD-Y123
$\text{Y}_{1-x}\text{Ca}_x\text{Ba}_2\text{Cu}_3\text{O}_{6+\delta}$	CD-YCa123
$(\text{Ca}_{1-x}\text{La}_x)(\text{Ba}_{1.75-x}\text{La}_{0.25+x})\text{Cu}_3\text{O}_{6+\delta}$	CLBLCO
$\text{CaLaBaCu}_3\text{O}_{6+\delta}$	CLBCO
$\text{Bi}_2\text{Sr}_2\text{CaCu}_2\text{O}_{8+\delta}$	OD-Bi2212
$\text{Bi}_2\text{Sr}_2(\text{Ca}_{1-x}\text{Y}_x)\text{Cu}_2\text{O}_{8+\delta}$	CD-Bi2212
$\text{HgBa}_2\text{CaCu}_2\text{O}_{6+\delta}$	OD-Hg1212
$(\text{Hg}_{0.5}\text{Fe}_{0.5})\text{Ba}_2(\text{Ca}_{1-x}\text{Y}_x)\text{Cu}_2\text{O}_{6+\delta}$	CD-HgFe1212
$\text{Tl}(\text{BaSr})\text{CaCu}_2\text{O}_{6+\delta}$	CD-Tl1212
$(\text{Tl}_{0.5+x}\text{Pb}_{0.5-x})\text{Sr}_2(\text{Ca}_{1-y}\text{Y}_y)\text{Cu}_2\text{O}_{6+\delta}$	CD-TlPb1212
(Triple-layer HTS)	
$\text{Bi}_2\text{Sr}_2\text{CaCu}_3\text{O}_{10+\delta}$	OD-Bi2223
$\text{HgBa}_2\text{Ca}_2\text{Cu}_3\text{O}_{8+\delta}$	OD-Hg1223
$\text{TlBa}_2\text{Ca}_2\text{Cu}_3\text{O}_{8+\delta}$	OD-Tl1223
$(\text{Cu}_{1-x}\text{Ca}_x)\text{Ba}_2\text{Ca}_2\text{Cu}_3\text{O}_{8+\delta}$	CD-CuCa1223
$(\text{Cu}_{1-x}\text{C}_x)\text{Ba}_2\text{Ca}_2\text{Cu}_3\text{O}_{8+\delta}$	CD-CuC1223

TABLE II: The experimental probes and their notations for the present work.

Experimental probe	Notation
resistivity	ρ
a -axis resistivity	ρ_a
c -axis resistivity	ρ_c
in-plane resistivity	ρ_{ab}
inflection point of $\rho(T)$	$d^2\rho/dT^2$
thermoelectric power	TEP or S
TEP at 290 K	S^{290}
a -axis TEP	S_a
in-plane TEP	S_{ab}
susceptibility	χ
susceptibility (H// c)	χ_c
susceptibility (H// ab)	χ_{ab}
nuclear magnetic resonance	NMR
nuclear quadrupole resonance	NQR
spin-lattice relaxation rate (NQR)	$(T_1T)^{-1}$
NMR knight shift (H// c)	K_c
angle-resolved photoemission spectroscopy	ARPES
angle-integrated photoemission spectroscopy	AIPES
superconductor-insulator-superconductor tunneling	SIS
superconductor-insulator-normal metal tunneling	SIN
near edge x-ray absorption fine structure	NEXAFS
electronic specific heat coefficient	γ
thermal conductivity	κ
neutron scattering	<i>neutron</i>
electronic Raman scattering	<i>ERS</i>
quasiparticle relaxation rate	<i>QPR</i>
polar angular magnetoresistance oscillations	<i>AMRO</i>

TABLE III: The $T_c^{max.}$ and $P_{pl}^{opt.}$ for single-layer HTSs plotted in Figs. 1(a) - 1(c).

HTS	$T_c^{max.}$ (K)	$P_{pl}^{opt.}$	Ref(s).
SrD-La214	39.4	0.16	27
SrD-La214	37	0.16	28
SrD-La214	36	0.16	29
SrD-La214	38	0.16	30
OD-Hg1201	97	0.235	31,32
CD-Bi2201	35.5	0.28	33
CD-Bi2201	33	0.28	34
OD-Tl2201	93 ^a	0.25 ^a	7,35,36

^aWe use the reported highest $T_c = 93$ K as $T_c^{max.}$ (Ref. 37). From the plot of T_c vs P_{pl} in Fig. 1(a), the optimal P_{pl} is estimated to be ~ 0.25 . The detail is in the text.

relationship is built on the sound experimental observations, which is similar to the situation of the most popular P_{T_c} -scale, although it is still mainly empirical and waited to be theoretically justified. Since the average area per copper in the CuO_2 -plane is almost independent of the HTS materials, therefore, P_{pl} is essentially equal to 2D hole-doping concentration defined as the hole-doping content per unit area. Using the 2D P_{pl} -scale, it was found in the phase diagram for all major HTSs plotted as a function of P_{pl} that the T^* -curves are independent of the n_{layer} while the T_c -curve strongly depends on it.²⁴ Therefore the P_{pl} -scale is intrinsically consistent with the pseudogap energy scale.²⁴ We can also extend the hole-doping content per CuO_2 plane to an effective 3D hole-doping content per CuO_2 block, which includes the oxygen coordination around the plane, (P_{3D}) by a simple conversion formula $P_{3D} \equiv P_{pl} \times (n_{layer}/V_{u.c.})$, where $V_{u.c.}$ is the unit cell volume.²⁵ Since P_{3D} is essentially the hole-doping content per unit volume, therefore, this natural extension of P_{pl} -scale to P_{3D} (P_{3D} -scale) has allowed us to address the corresponding 3D properties.²⁵ For instance, in the case of the single-layer HTS, the Hall number per " cm^3 ", calculated from the in-plane Hall coefficient, is not scaled with P_{pl} but P_{3D} .²⁵ The $\tau_c(T_c)$, a reduced temperature-scale defined as $\tau_c(T) \equiv T/T_c^{max.}$, of the single-layer HTS universally appears at $6 \times 10^{20} \text{ cm}^{-3}$ and reaches the $T_c^{max.}$ at $1.6 \times 10^{21} \text{ cm}^{-3}$ as shown in Fig. 1(b),²⁵ although their critical hole-doping concentrations on the P_{pl} -scale depend on the materials as shown in Fig. 1(a).²⁴ Thus, it was shown that various normal and superconducting properties for many different material systems can be consistently compared by using either P_{pl} or P_{3D} .^{24,25,26}

In order to reveal the intrinsic generic electronic properties of all HTSs, it is necessary to be able to put both 2D and 3D physical properties on a single phase diagram. To achieve this goal, we need a carrier-scale that is not only independent of the material system but also independent of the dimensionality of the physical properties.

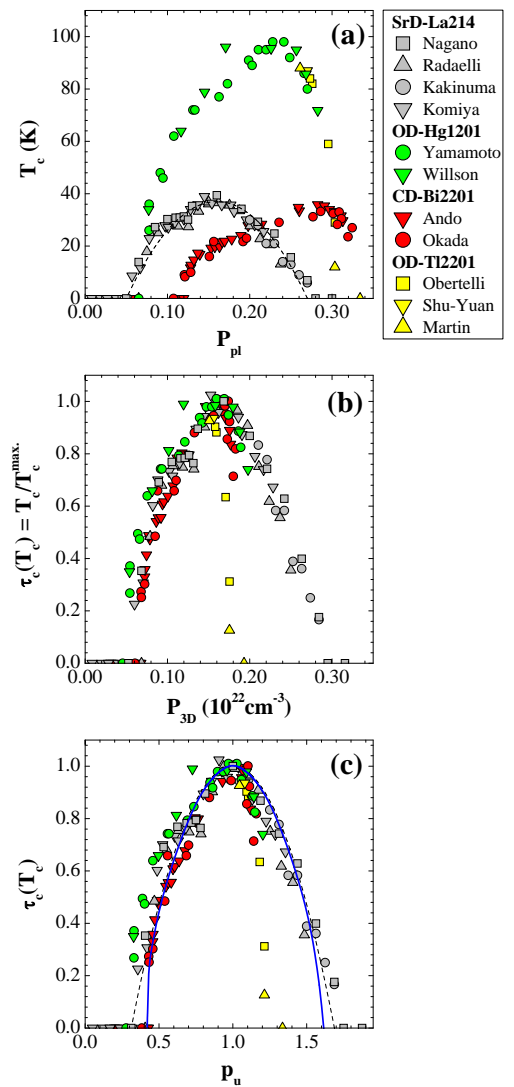


FIG. 1: (Color online) For the single-layer HTSs, (a) the superconducting transition temperature (T_c) as a function of P_{pl} , (b) the reduced superconducting transition temperature $\tau_c(T_c) (\equiv T_c/T_c^{max.})$ as a function of the effective 3D hole-doping concentration P_{3D} , and (c) the $\tau_c(T_c)$ as a function of P_{3D} . The plotted data are summarized in the Table III. The broken line comes from the equation (1). The solid line is our superconducting dome.

This can be achieved if, for each material system, we scale P_{pl} and P_{3D} with their corresponding optimal doping concentrations, $P_{pl}^{opt.}$ and $P_{3D}^{opt.}$, respectively. Here, we introduce a dimensionless unified hole-doping concentration, p_u ($p_u \equiv P_{pl}/P_{pl}^{opt.} = P_{3D}/P_{3D}^{opt.}$). This unified hole-doping scale (p_u scale) can be used for all physical properties, which is independent of their dimensionality, in all HTSs. Indeed, the identical doping dependent behaviors are preserved even though $\tau_c(T_c)$ of the single-layer HTS plotted as a function of P_{3D} in Fig. 1(b) was replotted as a function of p_u in Fig. 1(c).^{7,27,28,29,30,31,32,33,34,35,36} Here, each

$P_{pl}^{opt.}$ was determined from the plot of T_c vs P_{pl} for the each compound in the present work or Refs. 24,25,26. For the OD-Tl2201 there was few reports on the optimally doped samples because the optimally doped OD-Tl2201 is hard to prepare. In this case we use the highest $T_c = 93$ K among the published data as $T_c^{max.}$ ³⁷ From the plot of T_c vs P_{pl} in Fig. 1(a), the optimal P_{pl} is estimated to be ~ 0.25 . They are summarized in Table III. Essentially we can view p_u as a scaled dimensionality- and material-independent universal carrier-doping concentration that preserves the intrinsic doping dependency for **any** physical property for **all** HTSs. In this paper, we have analyzed the characteristic temperatures and energies observed in the 27 HTSs by 15 different experimental probe as a function of p_u . We find a dopant-specific unified electronic phase diagram for HTS. The dominate phase diagram is an asymmetric half-dome-shaped T_c -curve for the cation and anion (oxygen) co-doped (CD) HTS. T_c for the purely oxygen-doped (OD) HTS also follows the half-dome-shaped T_c curve with some indication of the influence of the thermally induced oxygen redistribution.

II. ANALYSIS

The details of how the P_{pl} - and P_{3D} -scales were constructed had been reported in Refs. 24 and 25, respectively. The determination of P_{pl} based on TEP is most reliable. Accordingly, the data including TEP are selected among the accumulated published data. The second reliable determination of P_{pl} is determined from the value of T_c using T_c vs P_{pl} curve for each compound reported in Refs. 24,25,26. When the data with P_{T_c} is analyzed, as the third method of determining P_{pl} , the P_{pl} is converted from P_{T_c} by using the relation in Fig. 2(c) discussed below. To clearly label how P_{pl} was determined for each sample or data set used in this paper, we use the following character to designate such that I to be the second method if the cited data have no TEP but T_c and II to be the third method if the cited data has only P_{T_c} . This designation to indicate the origin of the P_{pl} will be used in Table V - IX and in Figs. 3 - 6. We will use no designation whenever P_{pl} is directly determined from the TEP. All the HTSs used in the present analysis are summarized in Table I.

We examine various characteristic temperatures and energies of HTSs for constructing the phase diagram. The pseudogap is generally observed as the characteristic temperature derived by a scaling of the temperature dependence, as a distinct change in the slope of the temperature dependence or as a peak value in the energy-dispersion at a fixed temperature. Therefore, a reliable estimation can only be achieved through using a wide temperature or energy range. We only chose the characteristic temperatures and energies obtained by direct observation or those obtained through careful analysis of the data covering a wide temperature or energy range. For example, when T^* is derived by the scaling of the

TABLE IV: The HTSs plotted in Figs. 2(a) and 2(b).

n_{layer}	HTS	TEP	Ref(s).
1	SrD-La214	S	29,96,97,98,99,100
	SrD-La214	S_{ab}	101
	SrD-La214	S_a	102
	BaD-La214	S	103
	OD-La214	S_{ab}	104
	CeD-NdSr214	S	105
	SrD-LaNd214	S	106
	CD-Bi2201	S	107,108
2	CaD-Y1236	S	24
	OD-Hg1212	S	54
	CD-HgFe1212	S	52
3	OD-Hg1223 (underdoped)	S	54

temperature dependence observed below 300 K, T^* 's over 300 K is not used.

The pseudogap was first noticed as the temperature showing a broad maximum in $(T_1T)^{-1}$ vs T curve.⁸² The characteristic temperatures are observed as a broad maximum in the temperature dependence of the S vs T ,⁸ and γ vs T .⁶⁵ $S(T)$ can be scaled by $S(T_S^*)$ and T_S^* .²⁴ The resistive pseudogap temperature (T_ρ^*) is defined as a temperature where the resistivity bends downward from the linear temperature dependence at the high temperature.⁶⁰ The similar characteristic temperatures are observed also in χ vs T .⁶¹ The pseudogap by the QPR is observed as the gap-like behavior in substantial transient change of the optical transmission or reflection induced by ultrashort laser pulse photoexcitation.⁶⁶ The ARPES and tunneling experiments provide us with the characteristic energies and temperatures, such as the peak and hump energies observed in the energy-dispersion at a fixed temperature and the temperature dependence of the energy-dispersion curve, respectively.⁷⁶ The ERS give as the coherent and two-magnon peaks.²² In the NMR knight shift, T_{mK}^* is a temperature where the constant K_c at high temperature bends downward, and T_K^* is a temperature where the linear K_c below T_{mK}^* bends downward.^{84,85} Recently the resistivity curvature mapping based on the data of in-plane resistivity up to 300 K showed that there are two inflection points, the upper inflection point and the lower inflection point, which are identified in the ρ vs T curve far above T_c .⁶⁴ Therefore, there are various characteristic temperatures and/or energies reported in the literature. Our goal is to see if we can put all of them into one unified phase diagram.

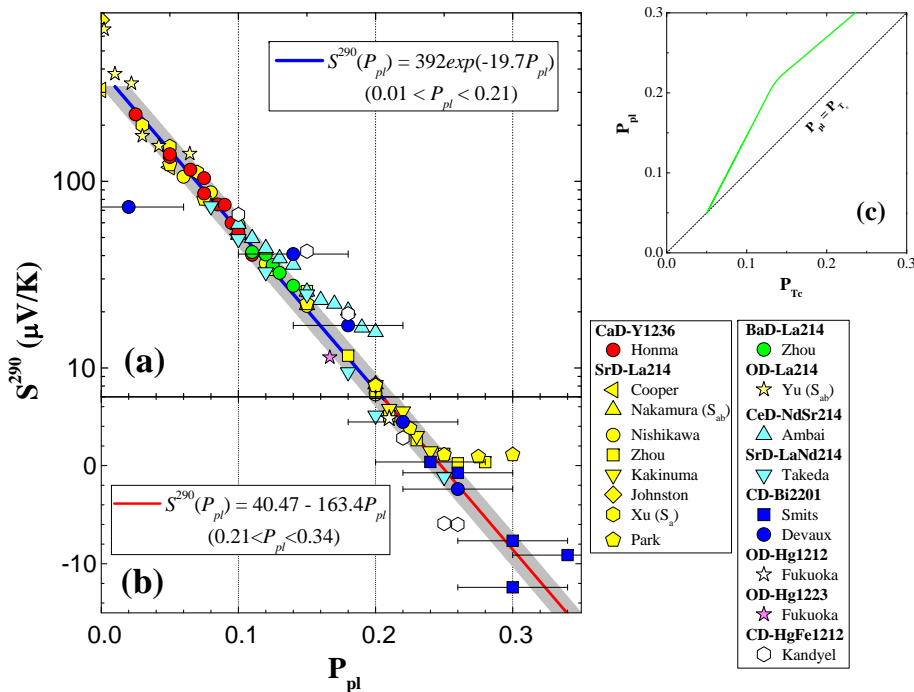


FIG. 2: (Color online) S^{290} as a function of the hole-doping content per CuO_2 plane. (a) $S^{290} (\geq 7 \mu\text{V/K})$ on the upper panel is plotted on a logarithmic scale, while (b) $S^{290} (< 7 \mu\text{V/K})$ on the lower panel is plotted on a linear scale. The plotted data are summarized in the Table IV. (c) Quantitative comparison between P_{pl} and P_{Tc} . The dotted line shows $P_{pl} = P_{Tc}$. We used this relation for the conversion from P_{Tc} into P_{pl} . The error of P_{pl} is below 0.04 for the CD-Bi2201 and below 0.01 for all other HTSs. The error bar for the other materials is not shown. The shaded area represents a region with the P_{pl} -error of ± 0.01 around the universal $S^{290}(P_{pl})$ -curve.

III. RESULTS AND DISCUSSION

A. Universal hole-doping scale

First of all, we demonstrate how the hole-doping scale based on the S^{290} is effective and universal. In Figs. 2(a) and (b), we plot S^{290} of sintered sample and S_{ab}^{290} of the single crystal as a function of P_{pl} , together with previously reported data.²⁴ $S^{290} (\geq 7 \mu\text{V/K})$ on the upper panel is plotted on a logarithmic scale, while $S^{290} (< 7 \mu\text{V/K})$ on the lower panel is plotted on a linear scale. In Figs. 2(a) and (b), the five single-layer, one double-layer, and one triple-layer HTSs are the newly added data points. They have been plotted with the previous reported SrD-La214 and CaD-Y1236. The plotted data are listed in Table IV. P_{pl} of SrD-La214 without excess oxygen is equal to Sr-content.⁴ The P_{pl} of CaD-Y1236, which the oxygen-content was determined to be 6 by the iodometric titration in Ar gas,²⁴ can be ambiguously and directly determined as a half of Ca-content, since the CaD-Y1236 has the isolated Cu layer in stead of CuO chain. In fact, it is shown by the O 1s and Cu 2p NEX-AFS experiment that the holes introduced by replacing

Y^{3+} with Ca^{2+} appear solely in the CuO_2 planes without affecting the isolated Cu layers in the CaD-Y1236.⁴¹ P_{pl} for the other materials were determined from the copper valency measured by the iodometric titration for the OD-La214¹⁰⁴ and CD-Bi2201,^{107,108} and the double iodometric titration for the OD-Hg1212,⁵⁴ CD-HgFe1212,⁵² and OD-Hg1223.⁵⁴ The error of P_{pl} is mainly coming from the oxygen-deficient (δ). For the double- and triple-layer HTSs, the error of δ was below 0.01.^{24,52,54} For the SrD-La214, the oxygen deficient is estimated to be ~ 0.005 , according to the result of Radaelli *et al.*²⁸ These error of P_{pl} can be estimated to be below 0.01. For the CD-Bi2201, the error of δ is ~ 0.02 ,^{107,108} and therefore the error of P_{pl} is ~ 0.04 . Noticed that the plotted data follow the universal $S^{290}(P_{pl})$ -curve proposed in Ref. 24, which is irrespective of the nature of dopant, n_{layer} , the structure and the sample quality, namely, single crystal or not. It is also independent from whether the CuO_2 plane is surrounded by the octahedral or pyramidal oxygen coordination. For the SrD-La214, there is the upward deviation from the universal line at $P_{pl} > 0.25$. This deviation is considered to be due to the oxygen-deficient that was reported to be significant over $x = P_{pl} \sim 0.25$.²⁸ In the CeD-NdSr214, the upward deviation over $P_{pl} \sim$

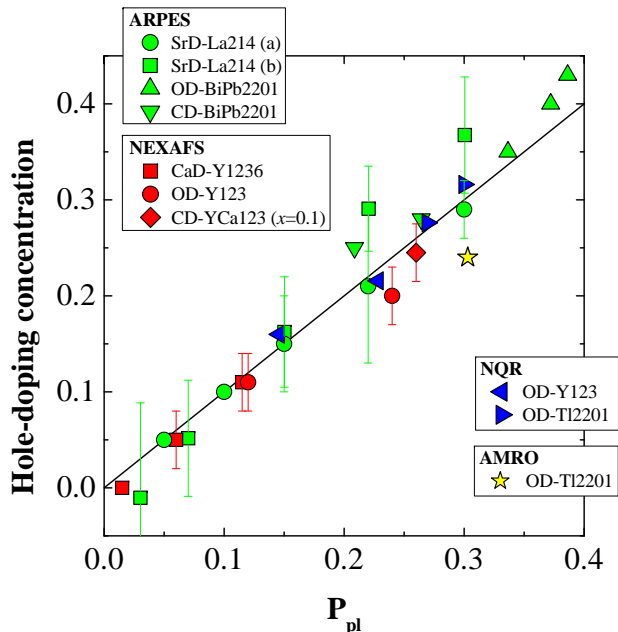


FIG. 3: (Color online) Hole-doping concentration determined by various techniques as a function of P_{pl} . The plotted data are summarized in Table V.

0.15 from the universal line can be explained by the oxygen deficiency generating the hole deficient of ~ 0.05 as pointed out in Ref. 105. Accordingly, all plotted data lie in a shaded area around our universal $S^{290}(P_{pl})$ -curve with the P_{pl} -accuracy of ± 0.01 within the reported error. Therefore, the proposed universal $S^{290}(P_{pl})$ -curve that purely based on the experimental grounds works well as the empirical intrinsic hole-scale for the HTS in the range of $0.01 < P_{pl} < 0.34$. In Fig. 2(c), we compare P_{pl} with P_{T_c} . The solid line shows P_{pl} as a function of P_{T_c} . The broken line shows $P_{pl} = P_{T_c}$. The quantitative difference between the P_{pl} scale and P_{T_c} scale becomes clear in Fig. 2(c). In addition we used this relation for the conversion from P_{T_c} into P_{pl} when the data plotted here have the P_{T_c} without TEP.

Next, we compare our universal scale based on the S^{290} to that determined by other techniques. The hole-doping concentration by ARPES (P_{ARPES}) is deduced from the area of the experimental Fermi surface (FS). The planar hole-doping concentration is also determined by NEXAFS (P_{NEXAFS}), by NQR (P_{NQR}) and by AMRO (P_{AMRO}). In Fig. 3, we plot the P_{ARPES} , P_{NEXAFS} , P_{NQR} and P_{AMRO} as a function of P_{pl} . The plotted data are summarized in Table V. It can be clearly seen that the P_{pl} determined by TEP is quite consistent with P_{NEXAFS} and P_{NQR} . Although there is a slight scattering, P_{pl} is also consistent with P_{ARPES} and P_{AMRO} .

TABLE V: The data plotted in Fig. 3.

Probe	HTS	P_{pl}	Ref.
ARPES	SrD-La214 (a)		38
	SrD-La214 (b)		39
	OD-BiPb2201		40
	CD-BiPb2201		40
NEXAFS	CaD-Y1236		41
	OD-Y123	I	41
	CD-YCa123 ($x=0.1$)	I	41
NQR	OD-Y123	I	42
	OD-Tl2201	I	42
AMRO	OD-Tl2201	I	43

Thus, our P_{pl} -scale is consistent with above other scales. Accordingly, the present p_u scale is also intrinsically consistent with the hole-doping concentrations determined by the above techniques.

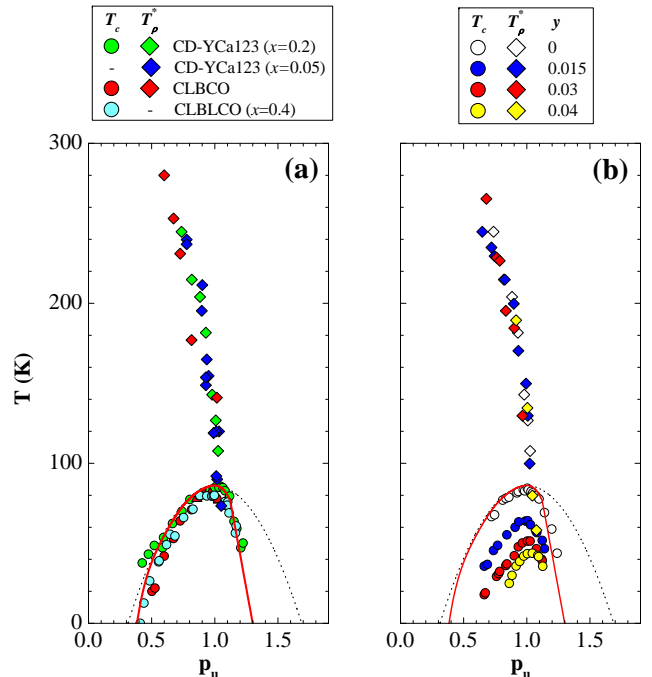


FIG. 4: (Color online) T_c and T_ρ^* as a function of p_u for (a) the OD-Y123-related materials and (b) $Y_{0.8}Ca_{0.2}Ba_2(Cu_{1-y}Zn_y)_3O_{6+\delta}$. The plotted data are summarized in Table VI. The solid line is a half-dome-shaped T_c -curve with $T_c^{max} = 86$ K. The dotted line comes from the equation (1) with $T_c^{max} = 86$ K.

B. Asymmetric half-dome-shaped T_c curve

In Fig. 4(a), we plot the T_c and T_ρ^* of all the OD-Y123 related materials which do not have significant contribution of CuO chain as a function of p_u . It includes CD-YCa123,^{6,8,44} CLBLCO,⁴⁵ and CLBCO.⁴⁶ First, we note that the $T_c(p_u)$ does not follow the well-known superconducting dome, as shown as a dotted line in Fig. 4(a), instead, it follows an asymmetric half-dome-shaped curve shown as a solid line. Although T_c in the underdoped regime basically follows the superconducting dome, T_c in the overdoped regime decreases much more rapidly. In Fig. 4(a), T_ρ^* decreases with doping, smoothly merges into the half-dome-shaped T_c curve and finally tends to reach an end point located at $(p_u, T) = (1.3, 0)$. Therefore, in contrast to the proposal that the T_ρ^* curve crosses the T_c curve,¹ the T_ρ^* curve smoothly merges into the T_c curve in the overdoped regime. In Fig. 4(b), we plot T_c and T_ρ^* as a function of p_u for $Y_{0.8}\text{Ca}_{0.2}\text{Ba}_2(\text{Cu}_{1-y}\text{Zn}_y)_3\text{O}_{6+\delta}$ for $0 \leq y \leq 0.04$.⁶ Although $T_\rho^*(p_u)$ slightly depends on Zn-content in the overdoped regime, $T_\rho^*(p_u)$ again tends to merge into $T_c(p_u)$ at the overdoped regime. This should be compared to the original plot, based on the P_{T_c} -scale, in which T_ρ^* crossed the superconducting dome and reached zero at a proposed QCP ($P_{T_c} = 0.19$).⁶ Accordingly, the crossing was an artifact that came from two sources; one is the use of a hole-scale that failed to taking into account the differences in dimensionality of different physical properties, namely, the two-dimensional T_ρ^* vs three-dimensional T_c , **and** the other is that the T_c curve for the majority of HTS follows the asymmetric dome-shaped curve, **only** SrD-La214 follows the symmetric dome-shaped T_c curve or superconducting dome.

$\tau_c(T_c)$ vs p_u plot for the cation and oxygen co-doped HTS and the purely oxygen-doped HTS are shown in Figs. 5(a) and (b), respectively. For comparison, $\tau_c(T_c)$ vs P_{pl} curve of OD-Y123 reported in Ref. 26 is also plotted in Fig. 5(b). $T_c^{max.}$ and $P_{pl}^{opt.}$ are summarized in Table VII. The CD-HTSs follow the present asymmetric half-dome-shaped T_c -curve. $\tau_c(T_c)$ vs p_u curve of the single-layer OD-Tl2201, which behaves differently from that of the other in the plot of T_c vs P_{3D} as shown in Fig. 1(b),²⁵ actually follows the asymmetric half-dome shaped T_c -curve. The other overdoped OD-HTSs also

follow the half-dome-shaped T_c curve. Note that T_c of the underdoped OD-HTS is slightly enhanced from the half-dome shaped T_c -curve and T_c appears at a lower p_u . The OD-Y123 also shows the similar trend, although it is influenced by the CuO chain ordering.²⁶ We attribute this to the influence of the soft oxygen dopants.¹⁰⁹ Thus, opposite to the common belief, the $\tau_c(T_c)$ vs p_u phase diagram of the majority of HTSs follow the asymmetric half-dome shaped T_c curve. Noticed that the asymmetric half-dome-shaped T_c curve goes to zero at $p_u \sim 1.3$. It is interesting to point out that if we take $P_{pl}^{opt.}$ to be universally equal to 0.16, as assumed in the P_{T_c} scale, then the critical $p_u \sim 1.3$ corresponds to $P_{T_c} \sim 0.2$ in the P_{T_c} scale. This value is very close to the proposed QCP ($P_{T_c} = 0.19$) identified by various experiments on the P_{T_c} -scale.^{1,6} Therefore this critical doping concentration is not located inside the superconducting phase and, physically, it is the doping concentration where all the phenomenology of high T_c ceases to exist and the ground state becomes a conventional Fermi liquid (FL) for $p_u > 1.3$.

In the overdoped triple-layer HTS, the charge density of the inner and outer planes were reported to be inhomogeneous.¹¹⁰ This is consistent with the $\tau_c(T_c)$ vs p_u behavior of OD-Bi2223, black triangles in Fig. 5(b), that T_c shows a flat region in the overdoped regime.⁵⁶ However, the $\tau_c(T_c)$ vs p_u behaviors of CD-CuCa1223,⁵³ and CD-Cu1223⁵³ plotted into Fig. 5(a) show the same trend as that of the single- and double-layer CD-HTSs. $\tau_c(T_c)$ vs p_u of OD-Tl1223,⁵⁸ and OD-Hg1223^{54,57} plotted in Fig. 5(b) also show the identical trend as that of the single- and double-layer OD-HTSs. Accordingly, although counter-intuitive, the charge density of the inner and outer planes of these materials is expected to be the same.

C. Unified electroni phase diagram

We now examine various characteristic temperatures and energies for HTSs that fall into the asymmetric half-dome-shaped T_c curve. $T_c(P_{pl})$ depends on the n_{layer} , while the $T^*(P_{pl})$ is independent of it.²⁴ Therefore, we group the single- and double-layer HTSs with same $T_c^{max} \sim 90$ K together. We found in Ref. 24 that the various characteristic temperatures or pseudogap temperatures can be separated into two groups of the lower pseudogap temperature (T_{lp}^*) and upper pseudogap temperature (T_{up}^*). T_c and major characteristic temperatures, which includes T_{lp}^* and T_{up}^* , are plotted on the reduced temperature-scale as a function of p_u in Figs. 6(a), (c) and (e). The characteristic energies are plotted on a reduced energy-scale $\mu_c(E) \equiv E/k_B T_c^{max}$, where k_B is Boltzmann's constant, as a function of p_u in Figs. 6(b), (d) and (f). We will call the four solid curves from the top to bottom the hump temperature (T_{hump}^*), T_{up}^* , T_{lp}^* and T_c curves in the temperature-scale, and the hump energy (E_{hump}^*), the upper pseudogap energy (E_{up}^*), the lower

TABLE VI: The data plotted in Figs. 4(a) and (b).

Fig.	HTS	P_{pl}	Ref(s).
4(a)	CD-YCa123 ($x=0.2$)		8,44
	CD-YCa123 ($x=0.05$)	II	6
	CLBLCO ($x=0.4$)		45
	CLBCO		46
4(b)	$Y_{0.8}\text{Ca}_{0.2}\text{Ba}_2(\text{Cu}_{1-y}\text{Zn}_y)_3\text{O}_{6+\delta}$ ($0 \leq y \leq 0.04$)	II	44

pseudogap energy (E_{lp}^*) and Δ_c -curves in the energy-scale, respectively. The E_{hump}^* , T_{up}^* , T_{lp}^* and T_c -curves are directly determined from the plotted data. The T_{hump}^* , E_{up}^* , E_{lp}^* and Δ_c curves are converted from the E_{hump}^* , T_{up}^* , T_{lp}^* and T_c curves using a relation of $T = E/zk_B$ or $E = zk_B T$ for each characteristic energy or temperature. In the energy-scale, the solid curves correspond to $z = 3.5$ and gray zone shows the energy range from $3k_B T$ to $4k_B T$.

First, we summarize the characteristic temperatures and energies derived from the transport and thermodynamic properties in Figs. 6(a) and (b). Here, the plotted

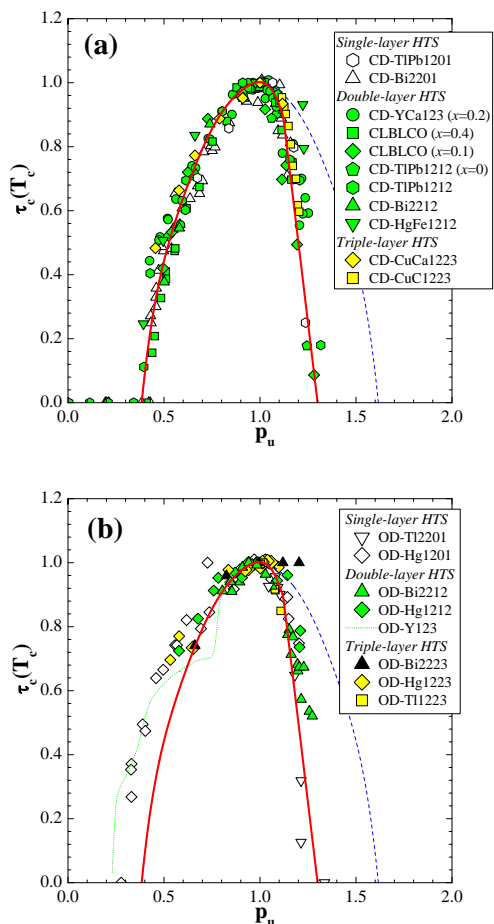


FIG. 5: (Color online) Extended unified electronic phase diagram plotted as $\tau_c(T_c)$ vs p_u for (a) the cation and oxygen co-doped HTS's and (b) the purely oxygen doped HTS. The plotted data are summarized in Table VII. The solid and broken lines are an asymmetric half-dome-shaped T_c curve and our superconducting dome, respectively. The dotted line is the T_c curve for OD-Y123.²⁶

TABLE VII: The $T_c^{max.}$ and $P_{pl}^{opt.}$ for the HTSs plotted in Figs. 5(a) and 5(b).

Fig.	HTS	$T_c^{max.}$ (K)	$P_{pl}^{opt.}$	P_{pl}	Ref(s).
5(a)	(Single-layer HTS)				
	CD-TlPb1201	50	0.25		47
	CD-Bi2201	35.5	0.28		33
	CD-Bi2201	33	0.28		34
	(Double-layer HTS)				
	CD-YCa123 ($x=0.2$)	85	0.237		44,48
	CD-YCa123 ($x=0.2$)	81	0.238	II	6
	CD-YCa123 ($x=0.2$)	85.5	0.238		8
	CLBLCO ($x=0.4$)	81	0.235		45
	CLBLCO ($x=0.1$)	57.7	0.205		45
	CD-TlPb1212 ($x=0$)	- ^a	0.235		8
	CD-TlPb1212	94	0.235		49
	CD-Tl1212	90	0.235		36
	CD-Bi2212	92	0.236		50
	CD-Bi2212	81	0.238		51
	CD-HgFe1212	73	0.227		52
	(Triple-layer HTS)				
	CD-CuCa1223	122	0.248		53
CD-CuC1223	110	0.215		53	
5(b)	(Single-layer HTS)				
	OD-Tl2201	93 ^b	0.25 ^b		7,35,36
	OD-Hg1201	97	0.235		31,32
	(Double-layer HTS)				
	OD-Bi2212	92	0.238		7
	OD-Hg1212	127	0.227		54
	OD-Hg1212	125	0.227		55
	(Triple-layer HTS)				
	OD-Bi2223	108	0.215		56
	OD-Hg1223	135	0.215		54
	OD-Hg1223	138	0.215		57
	OD-Tl1223	128	0.23		58

^aThe $T_c/T_c^{max.}$ was reported.

^bWe use the reported highest $T_c = 93$ K as $T_c^{max.}$ ³⁷ From the plot of T_c vs P_{pl} in Fig. 1(a), the optimal P_{pl} is estimated to be ~ 0.25 . The detail is in the text.

data are summarized in Table VIII. T^* 's determined from TEP and γ lie on the T_{lp}^* -curves, while T^* 's determined from ρ and QPR lie on the T_{up}^* curves, as reported in Ref. 24. Accordingly, the upper pseudogap is identified by the ρ and QPR, and the lower pseudogap is identified by TEP and γ experiments. However, T^* determined from the ρ_c tends to be higher than T_{up}^* , although the doping range is restricted. This may suggest a third pseudogap as already pointed out in Ref. 24. This suggestion is further supported by the similar behavior derived by other probes in the temperature- and energy-scales. We plot the upper and lower inflection points of ρ_a of OD-Y123 into the Fig. 6(a).⁶⁴ The lower and upper inflection points

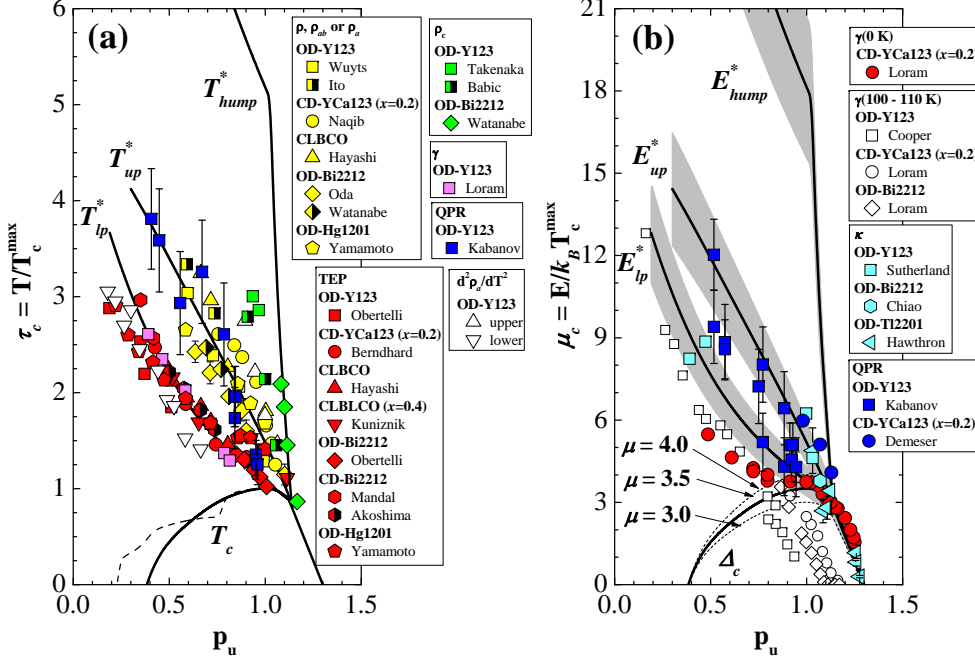


FIG. 6: (Color online) Unified electronic phase diagram for the single- and double-layer HTS's with $T_c^{max} \sim 90$ K. The temperature- and energy-scale for the pseudogap and superconducting gap obtained from transport properties are summarized in Figs. 6(a) and 6(b), from the spectroscopy properties in Figs. 6(c) and (d), and from NMR, QPR and scattering properties in Figs. 6(e) and 6(f), respectively. For Fig. 6(a) and 6 (b), the plotted data are summarized in the Table VIII. For Figs. 6(c) - 6(f), the plotted data are summarized in the Table IX. The E_{hump}^* , T_{up}^* , T_{lp}^* , and T_c curves are directly determined from the plotted data. The T_{hump}^* , E_{up}^* , E_{lp}^* , and Δ_c curves are calculated from the E_{hump}^* , T_{up}^* , T_{lp}^* , and T_c -curves using a relation of $T = E/zk_B$ or $E = zk_B T$, respectively. The broken lines show the T_c curve or Δ_c curve for OD-Y123. In the energy-scale, the solid lines corresponds to $z = 3.5$ and gray zone shows the energy range from $3k_B T$ to $4k_B T$.

seem to lie on the T_{lp}^* and T_{up}^* curves, respectively.

For the characteristic energies, we use the data reported in the γ ,^{67,68,69} κ ,^{10,11,70} and QPR experiment.^{66,71} E^* 's determined from the QPR lie on the E_{up}^* curve. E^* 's determined from κ show up on either E_{lp}^* or E_{up}^* curve. In the overdoped side, these E^* 's clearly merge into the Δ_c -curve. This indicates that there is no QCP inside the superconducting phase. In Fig. 6(b), the normal state gap, $E_{sh}^*(110\text{ K})$ and zero temperature superconducting gap, $E_{sh}^*(0\text{ K})$ determined by the specific heat measurement are plotted as the open symbols and solid circles, respectively.^{67,68,69} The $E_{sh}^*(110\text{ K})$ at $p_u < 0.85$ and $E_{sh}^*(0\text{ K})$ follows the E_{lp}^* - or $zk_B T_{lp}^*$ -curve. However, $E_{sh}^*(110\text{ K})$ at $p_u > 0.85$ deviates downward from the E_{lp}^* -curve, crosses the Δ_c -curve and finally goes to zero inside the Δ_c -curve. The temperature of $\sim 110\text{ K}$ ($\tau_c(110\text{ K}) = 110/90 \sim 1.2$)

corresponds to the T_{lp}^* at $p_u \sim 0.85$. The influence of the lower pseudogap on the extraction of E^* 's is clearly seen. The plotted $E_{sh}^*(110\text{ K})$ is the same data set used to support the existence of the QCP *inside* the superconducting phase on the P_{T_c} scale.¹ Accordingly, the existence of the QCP inside the superconducting phase is extrinsic to high T_c .

We summarize the characteristic temperatures and energies derived from the spectroscopic measurements in Figs. 6(c) and (d). The plotted data are summarized in Table IX. T^* determined in the AIPES lies on T_{hump}^* .¹² T^* determined from the ARPES,^{13,72,73} and SIS⁷⁴ cannot be grouped into either T_{up}^* or T_{lp}^* curve, since they lie between T_{up}^* and T_{lp}^* -curves. The E^* determined in the ARPES,^{13,14,15,73,75,76,77} and tunneling,^{16,17,74,78,79,80,81} are plotted in Fig. 6(d): the peak and hump energies

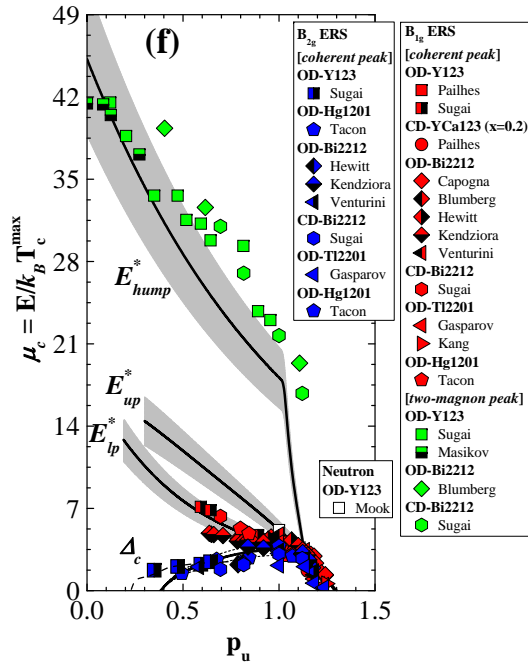
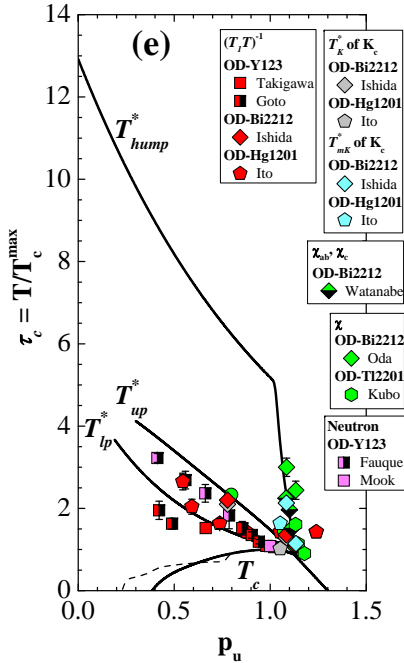
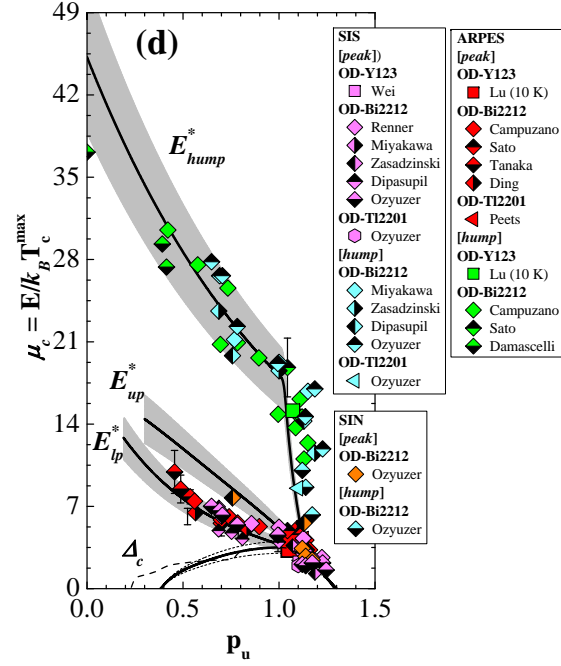
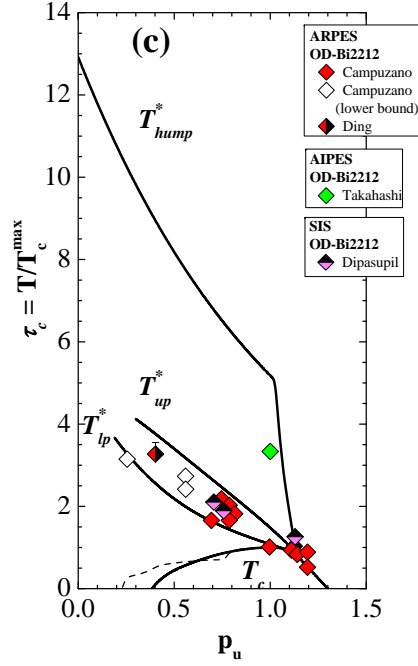


TABLE VIII: The HTSs plotted in Figs. 6(a) and 6(b).

Fig.	Probe	HTS	P_{pl}	Ref(s).
6(a)	ρ	OD-Y123	I	59
		CD-YCa123 ($x=0.2$)	II	6
		CLBCO		46
		OD-Hg1201		31
	ρ_a	CD-Bi2212		9
	ρ_{ab}	OD-Y123	I	60
		OD-Bi2212	I	61
	ρ_c	OD-Y123	I	62,63
		OD-Bi2212	I	9
	$d^2\rho_a/dT^2$	OD-Y123	I	64
	TEP	OD-Y123		7
		CD-YCa123 ($x=0.2$)		8
		CLBCO		46
		CLBLCO ($x=0.4$)		45
OD-Bi2212			7	
CD-Bi2212			50,51	
OD-Hg1201			31	
γ	OD-Y123	I	65	
QPR	OD-Y123	I	66	
6(b)	γ	CD-YCa123 ($x=0.2$)	I	67
		OD-Y123		68
		OD-Bi2212	I	69
	κ	OD-Y123	I	10
		OD-Bi2212	I	70
		OD-Tl2201	I	11
	QPR	OD-Y123	I	66
		CD-YCa123 ($x=0.2$)	I	71

observed in ARPES and tunneling lie on the E_{lp}^* and E_{hump}^* curves, respectively. It is clearly seen that there is a third energy scale corresponding to the hump structure observed in the ARPES and tunneling spectroscopy.

We summarize the characteristic temperatures and energies derived from the spin and charge probes in Figs. 6(e) and (f), respectively. The plotted data are summarized in Table IX. For the characteristic temperatures, T^* determined from the $(T_1T)^{-1}$ lies on the T_{lp}^* . T^* determined from the neutron lies between T_{up}^* - and T_{lp}^* curves. T_{mK}^* and T_K^* observed in K_c lie on the T_{hump}^* and T_{up}^* , respectively.^{84,85} For the characteristic energies, the half of the coherent peak energy of B_{2g} ERS,^{22,23,90,91,94,95} half of the coherent peak energy of B_{1g} ERS,^{19,20,21,22,23,88,89,90,91,92,93,94,95} and half of the two-magnon peak energy of B_{1g} ERS^{21,22,89} lie on the Δ_c , E_{lp}^* and E_{hump}^* curves, respectively.

From Figs. 6(a) – 6(f), we can conclude that the phase diagram fundamentally reproduces the T vs P_{pl} plot in Ref. 24. Their characteristic temperatures T^* lie on either the T_{up}^* or the T_{lp}^* curve in Ref. 24. Furthermore, the third characteristic energy, the “hump” energy, does

TABLE IX: The HTSs plotted in Figs. 6(c) - 6(f).

Fig.	Probe	HTS	P_{pl}	Ref(s).
6(c)	ARPES	OD-Bi2212	I	13,72,73
	AIPES	OD-Bi2212	I	12
	SIS	OD-Bi2212	I	74
6(d)	ARPES	OD-Y123	I	75
		OD-Bi2212	I	13,14,15,73,76
		OD-Tl2201	I	77
	SIS	OD-Y123	I	78
		OD-Bi2212	I	16,17,74,79,80
		OD-Tl2201	I	81
SIN	OD-Bi2212	I	17	
	$(T_1T)^{-1}$	OD-Y123	I	82,83
		OD-Bi2212	I	84
OD-Hg1201		I	85	
K_c	OD-Bi2212	I	84	
	OD-Hg1201	I	85	
neutron	OD-Y123	I	18,86	
χ	OD-Bi2212	I	61	
	OD-Tl2201	I	87	
χ_{ab} and χ_c	OD-Bi2212	I	9	
6(e)	B_{1g} ERS	OD-Y123	I	22,88,89
		CD-YCa123 ($x=0.2$)	I	88
		OD-Bi2212	I	20,21,23,90,91
		CD-Bi2212	I	92
		OD-Tl2201	I	93
		OD-Hg1201	I	94
	B_{2g} ERS	OD-Y123	I	22
		OD-Bi2212	I	23,90,91
		CD-Bi2212	I	22
		OD-Tl2201	I	95
	OD-Hg1201	I	94	
neutron	OD-Y123	I	18	

exist, although it is hard to detect as the corresponding characteristic temperature or T_{hump}^* . All four characteristic temperatures (T_c , T_{lp}^* , T_{up}^* , and T_{hump}^*) and the corresponding energies (Δ_c , E_{lp}^* , E_{up}^* , and E_{hump}^*) do not cross each other. The four temperatures and energies tend to converge with increasing p_u , merge at $p_u \sim 1.1$, and finally vanish at $p_u \sim 1.3$.

Some T^* 's (E^* 's) have relatively large scattering, and are hard to group into either T_{up}^* (E_{up}^*)-curve or T_{lp}^* (E_{lp}^*)-curve. For example, the E^* from κ and T^* from ARPES, tunneling spectroscopy and neutron scattering are scattered. These scattering may come from the differences in the characteristic time-scale and length-scale specific to different experimental probes for observing the intrinsically inhomogeneous electronic states, as discussed by Mihailovic and Kabanov.¹¹² Indeed, similar to T_{up}^* - and T_{lp}^* -curves or E_{up}^* - and E_{lp}^* -curves, they all be-

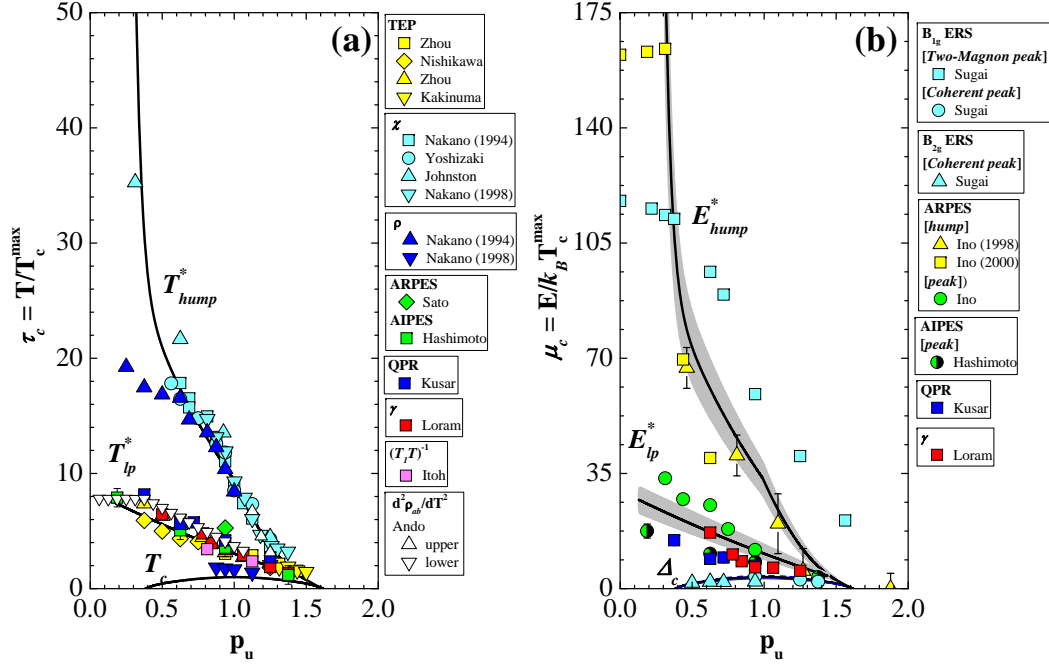


FIG. 7: (Color online) Electronic phase diagram for the single-layer SrD-La214. The temperature- and energy-scale for the characteristic temperatures and energies are summarized in Figs. 7(a) and (b), respectively. The plotted data are summarized in Table X.

come smaller and closer in the magnitude with increasing doping in the underdoped regime. They merge into T_c or Δ_c -curve in the overdoped regime and universally vanish at $p_u = 1.3$. The pseudogap, manifested either as the characteristic energy or characteristic temperature and independent of its origin, universally disappears at $p_u \sim 1.3$ together with the superconductivity. This strongly suggests that the pseudogap phase is the precursor of the superconducting phase.

In Fig. 8(a), we present a sketch of the unified electronic phase diagram for HTSs purely based on experimental grounds. The characteristic features of the unified electronic phase diagram for single- and double-layer HTSs with $T_c^{\max} \sim 90$ K are: (i) the asymmetric half-dome-shaped T_c -curve (SC phase), (ii) there are three characteristic temperatures, T_{hump}^* , T_{up}^* , and T_{lp}^* in the underdoped region ($p_u < 1$), (iii) all three characteristic temperatures and T_c come together at $p_u = 1.1$ in the overdoped region and vanish at $p_u = 1.3$, (iv) T_{hump}^* changes into the rapid decrease at $p_u \sim 1$, (v) T_{hump}^* and T_{lp}^* are concave upward, while the T_{up}^* is con-

cave downward, and (vi) the electronic phase diagram on the temperature-scale can be translated into that on the energy-scale through $E = zk_B T$ with $z = 3.5 \pm 0.5$. Although we use HTSs with $T_c^{\max} \sim 90$ K as our model system, we should emphasize that (i) – (vi) are salient features for all, except of SrD-La214 discussed in Sec. III E, HTSs. We will call this phase diagram the “unified electronic phase diagram (UEPD)” of HTS. Finally the T_{lp}^* - and T_{up}^* -curves tend to merge into the Néel temperature (T_N) curve with undoping.^{114,115}

D. Phase diagram for the SrD-La214

Now we discuss the HTS with symmetric T_c curve, i.e., the phase diagram of SrD-La214. For the SrD-La214, the characteristic temperatures on the reduced temperature-scale and characteristic energies on the reduced energy-scale are plotted as a function of p_u in Figs. 7(a) and (b), respectively. The plotted data are summarized in Table X. First, noticed that the characteristic temper-

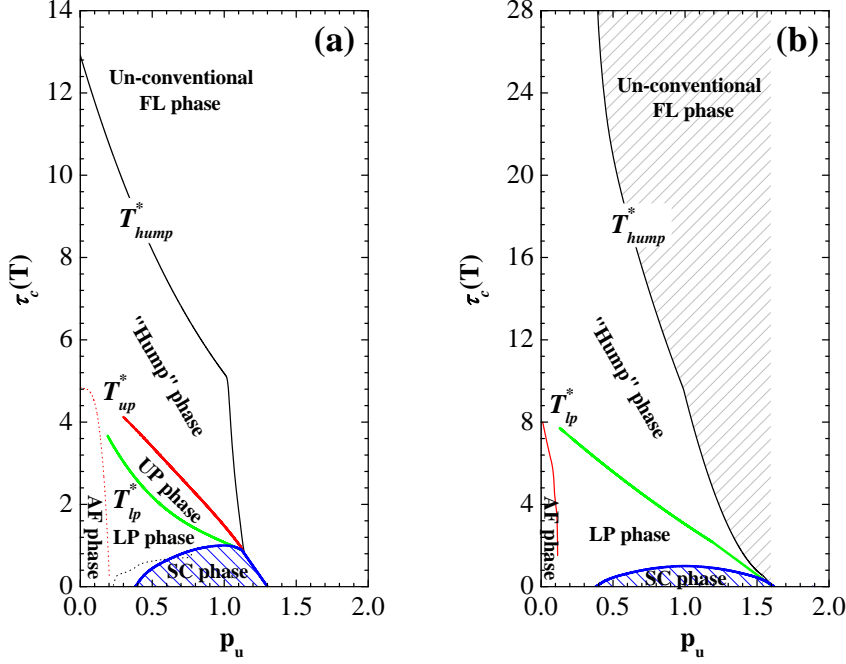


FIG. 8: (Color online) Sketches of (a) the UE PD for HTS with $T_c^{max} \sim 90$ K and (b) the phase diagram for the SrD-La214. In Fig. 8(a), the superconducting (SC) and antiferromagnetic (AF) phases represented by the dotted lines are coming from the OD-Y123.^{26,113} In Fig. 8(b), the AF phase for the SrD-La214 is cited from Refs. 114 and 115.

atures are separated into not three curves of T_{lp}^* , T_{up}^* and T_{hump}^* , but two curves. Also in the energy-scale, the characteristic energies are separated into two curves. In the UE PD, the T_{lp}^* - or E_{lp}^* -curve was defined by TEP , the peak structure of ARPES and tunneling, γ , and T_{hump}^* or E_{hump}^* curve was defined by the ρ_c , susceptibility, the hump structure of ARPES and tunneling, and two-magnon peak of B_{1g} ERS. In the SrD-La214, the lower curve of the temperature- or energy-scale is identified by TEP , the peak structure of ARPES and tunneling, γ , and the upper curve is identified by the χ , the hump structure of ARPES and tunneling, and two-magnon peak of B_{1g} ERS. Accordingly, the lower and upper curves of SrD-La214 are designated to be T_{lp}^* and T_{hump}^* (E_{lp}^* and E_{hump}^*), respectively. In the SrD-La214, the T^* or E^* defined by the ρ lie on either of the two curves, suggesting no T_{up}^* - or E_{up}^* curve. Because, in the UE PD, the T^* or E^* defined by the ρ and QPR lied on T_{up}^* or E_{up}^* curve. In fact, T_{ρ}^* 's for the SrD-La214 with $x < 0.16$ ($p_u < 1$) lie on the T_{hump}^* -curve,¹¹⁶ while T_{ρ}^* 's for $x > 0.14$ ($p_u > 0.875$) lie on the T_{lp}^* curve.¹²⁶ We also

plot the upper and lower inflection points of ρ_{ab} into the Fig. 7(a).⁶⁴ The upper and lower inflection points seem to correspond to the T_{hump}^* and T_{lp}^* curves, respectively. In the SrD-La214, the usual upper pseudogap temperatures identified in UE PD tend to lie on either lower pseudogap temperature or the hump temperature.

In Fig. 8(b), we present a sketch of the phase diagram for SrD-La214. The $T_c(p_u)$ follows a symmetric dome-shaped T_c -curve (SC phase). This is quite different from feature (i) of the UE PD. There are two characteristic temperatures, i.e., T_{hump}^* and T_{lp}^* , in the range from the underdoped regime. This is also different from feature (ii) above. T_{lp}^* of SrD-La214 seems to be a combination of T_{up}^* and T_{lp}^* of the UE PD. Although the T_c , T_{hump}^* and T_{lp}^* decreases with doping, there is no merging until the end point. This is also different from the feature (iii) above. T_c , T_{hump}^* , and T_{lp}^* fall down to $(p_u, \tau_c) = (1.6, 0)$ in contrast to $(1.3, 0)$ in the UE PD. There is a slight change in curvature in the $T_{hump}^*(p_u)$ at $p_u \sim 1$. This may share the same origin as the feature (iv) above, although it is much weaker in the SrD-La214 system.

Both features (v) and (vi) are similar to that of UEPD.

E. Comparison between the unified electronic phase diagram and the other phase diagram

The present UEPD is different from the phase diagrams that were proposed and discussed in Refs. 1,2,3 and 127. The phase diagram in Ref. 1 suggests that the single T^* curve crosses the dome-shaped T_c curve or superconducting phase at around the optimal doping level, and fall down to $T = 0$ at the QCP inside the superconducting phase. This phase diagram implies that there is no correlation between the pseudogap phase and high- T_c phase, and therefore the pseudogap is a pure competing order. The phase diagram of Ref. 2 suggests that the dome-shaped T_c curve intercepts the double T^* curves at around the optimal doping level. The upper and lower T^* curves are concave downward and upward, respectively. These phase diagram is based on the P_{T_c} -scale, since T_c follows the superconducting dome. The phase diagram on Ref. 3 shows a tendency that the double T^* curves merge into the asymmetric T_c curve at around the slightly overdoped level and go to zero with T_c at the end point. However, both T^* curves are concave downward. In Refs. 1,2,3, the pseudogap does not merge into the T_N curve with undoping. The phase diagram discussed in Ref. 127 shows that the single T^* -curve smoothly merges into the T_N -curve with undoping, and smoothly merges into the asymmetric T_c curve at the end point with doping. However, the single T^* curve is concave downward. Thus, without alluding to the microscopic picture for the high- T_c mechanism, all the previously proposed phase diagrams are different from our UEPD, except that the asymmetric T_c curve in Refs. 3 and 127 is similar to the present half-dome shaped T_c curve.

The present UEPD clearly appears that pseudogap exists above T_c for $p_u < 1.1$, while for $p_u > 1.1$ pseudo-

gap appears at T_c . Even experimental data that supported a QCP inside the superconducting dome on the P_{T_c} -scale followed the UEPD. The phase diagram for the SrD-La214 shows that pseudogap temperatures and corresponding characteristic energies always exist above the superconducting phase, until the pseudogap disappears together with the superconducting phase at $p_u = 1.6$. These results indicate that for all the HTSs the pseudogap phase always co-exists with the superconducting phase up to the end point and does not intersect the superconducting phase. Furthermore, the overdoped HTS with superconductivity cannot be regarded as a conventional FL phase, since there is always the pseudogap phase with superconducting phase. Both phase diagrams suggest no QCP inside the superconducting phase. Actually, it has reported that QCP may exist at around the end point of the superconducting phase when superconductivity has completely disappeared in CLBLCO,¹²⁸ SrD-La214,¹²⁹ OD-Tl2201,¹³⁰ and OD-Bi2212.¹³⁰

The UEPD is consistent with the idea that the pseudogap phase is, if not sufficient, necessary for the high T_c . It also implies that at least two distinct energy scales, i.e., pseudogap and superconductivity, are required to realize high T_c . If we adopt a scenario that superconducting pairing is realized in the pseudogap phase and the global phase coherence occurs at T_c , then the smooth merging of T^* 's and T_c in the overdoped regime suggests that cuprates become a “more conventional” superconductor. Because pairing and phase coherence occurs at the same temperature (T_c). However since pseudogap still exists, it simply merges with T_c and changes with T_c , therefore the superconducting state as well as the normal state are still “unconventional” up to the end point as reported in some studies.^{11,77} This also explains why the pseudogap phase was never observed in the overdoped regime except SrD-La214. Even in the SrD-La214, the observation of the pseudogap in the overdoped regime strongly depends on the experimental probe. For example, it is not observed in the resistivity measurements but can be clearly seen by magnetic susceptibility and TEP measurements, as shown in Fig. 7.

In the previous paper, we pointed out that the observed T_{lp}^* and T_{up}^* are coming from not one pseudogap, but two pseudogaps,²⁴ because the temperature where the TEP has the broad peak, corresponding to T_{lp}^* , was different from the temperature where the TEP starts to depend on the Zn-doping, corresponding to T_{up}^* .²⁴ However, according to the idea by Mihailovic and Kabanov,¹¹² we can not completely rule out a possibility that three characteristic temperatures, including T_{hump}^* , are of the same physical origin. The different characteristic temperatures may come from the differences in the characteristic time-scale and length-scale specific to different experimental probes for observing the intrinsically inhomogeneous electronic states or pseudogap phase.

TABLE X: The data plotted in Fig. 7 for SrD-La214.

Fig.	Probe	Ref(s).
7(a)	TEP	29,68,98,99
	χ	116,117,118,119
	ρ	116,119
	$d^2\rho_{ab}/dT^2$	64
	ARPES	120,121,122
	AIPES	123
	specific heat	48
	$(T_1T)^{-1}$	124
	7(b)	ARPES
QPR		125
γ		48
B_{1g} ERS		22
B_{2g} ERS		22

IV. SUMMARY

We have proposed a dimensionless hole-doping concentration (p_u), which is scaled by the optimal hole-doping concentration, for all HTSs, and construct a UEPD for almost all HTSs, except of the purely cation-doped SrD-La214. In the UEPD all experimentally observed characteristic temperatures and energies converge as p_u increases in the underdoped regime, they merge together with the T_c vs p_u curve at $p_u \sim 1.1$ in the overdoped regime and finally goes to zero at $p_u \sim 1.3$. On the other hand, for SrD-La214, although all experimentally observed characteristic temperatures and energies converge as p_u increases in the underdoped regime, they merge together with the T_c vs p_u curve at $p_u \sim 1.6$ where T_c goes to zero. However, the detection of pseudogap becomes subtle and probe dependent for $p_u > 1$. Both the UEPD and the phase diagram of SrD-La214 clearly show that the pseudogap phase is a precursor of high T_c . Finally, there remains a question of why the phase diagram for SrD-La214 is different from the UEPD. The UEPD is

based on the cation and oxygen co-doped HTS materials, while the SrD-La214 is the pure cation doped HTS. Although the pure oxygen-doped HTS also follows the UEPD, the phase diagram is slightly deformed by the influence of the thermally induced oxygen redistribution. Accordingly, although we can not pin down exactly why the SrD-La214 does not follow the UEPD, we speculate that the differences are coming from a combination of lattice response, such as octahedral tilt mode, to hole doping and the hard-dopant effect discussed in Ref. 109. Further studies are necessary to properly address this issue.

Acknowledgments

T.H. would like to thank M. Tanimoto of Asahikawa Medical College for offering relief-time for this study. P.H.H. is supported by the State of Texas through the Texas Center for Superconductivity at the University of Houston.

* Electronic address: honma@asahikawa-med.ac.jp

† Electronic address: phor@uh.edu

- ¹ J. L. Tallon, *Physica (Amsterdam)* **349C**, 53 (2001).
- ² B. Batlogg and V. J. Emery, *Nature* **382**, 20 (1996).
- ³ V. J. Emery, S. A. Kivelson and O. Zachar, *Phys. Rev. B* **56**, 6120 (1997).
- ⁴ J. B. Torrance, Y. Tokura, A. I. Nazzari, A. Bezinge, T. C. Huang and S. S. P. Parkin, *Phys. Rev. Lett.* **61**, 1127 (1988).
- ⁵ M. R. Presland, J. L. Tallon, R. G. Buckley, R. S. Liu and N. E. Flower, *Physica (Amsterdam)* **176C**, 95 (1991).
- ⁶ S. H. Naqib, J. R. Cooper, R. S. Isram and J. L. Cooper, *Phys. Rev.* **71**, 184510 (2005); S. H. Naqib, *Physica (Amsterdam)* **443C**, 43 (2006).
- ⁷ S. D. Obertelli, J. R. Cooper and J. L. Tallon, *Phys. Rev. B* **46**, 14928 (1992).
- ⁸ C. Bernhard and J. L. Tallon, *Phys. Rev. B* **54**, 10201 (1996).
- ⁹ T. Watanabe, T. Fujii and A. Matsuda, *Phys. Rev. Lett.* **84**, 5848 (2000).
- ¹⁰ M. Sutherland, D. G. Hawthorn, R. W. Hill, F. Ronning, S. Wakimoto, H. Zhang, C. Proust, E. Boaknin, C. Lupien, L. Taillefer, R. Liang, D. A. Bonn, W. N. Hardy, R. Gagnon, N. E. Hussey, T. Kimura, M. Nohara and H. Takagi, *Phys. Rev. B* **67**, 174520 (2003).
- ¹¹ D. G. Hawthorn, S. Y. Li, M. Sutherland, E. Boaknin, R. W. Hill, C. Proust, F. Ronning, M. A. Tanatar, J. Paglione, L. Taillefer, D. Peets, R. Liang, D. A. Bonn, W. N. Hardy, N. N. Kolesnikov, *Phys. Rev. B* **75**, 104518 (2007).
- ¹² T. Takahashi, T. Sato, T. Yokoya, T. Kamiyama, Y. Naitoh, T. Mochiku, K. Yamada, Y. Endoh, K. Kadowaki, *J. Phys. Chem. Solids* **62**, 41 (2001).
- ¹³ J. C. Campuzano, H. Ding, M. R. Norman, H. M. Fretwell, M. Randeria, A. Kaminski, J. Mesot, T. Takeuchi, T. Sato, T. Yokoya, T. Takahashi, T. Mochiku, K. Kadowaki, P. Guptasarma, D. G. Hinks, Z. Konstantinovic, Z. Z. Li and H. Raffy, *Phys. Rev. Lett.* **83**, 3709 (1999).
- ¹⁴ H. Ding, J. R. Engelbrecht, Z. Wang, J. C. Campuzano, S. -C. Wang, H. -B. Yang, R. Rogan, T. Takahashi, K. Kadowaki and D. G. Hinks, *Phys. Rev. Lett.* **87**, 227001 (2001).
- ¹⁵ K. Tanaka, W. S. Lee, D. H. Lu, A. Fujimori, T. Fujii, Risdiana, I. Terasaki, D. J. Scalapino, T. P. Devereaux, Z. Hussain and Z. -X. Shen, *Science* **314**, 1910 (2006).
- ¹⁶ N. Miyakawa, P. Guptasarma, J. F. Zasadzinski, D. G. Hinks and K. E. Gray, *Phys. Rev. Lett.* **80**, 157 (1998).
- ¹⁷ L. Ozyuzer, J. F. Zasadzinski, C. Kendziora and K. E. Gray, *Phys. Rev. B* **61**, 3629 (2000).
- ¹⁸ H. A. Mook, M. Yethiraj, G. Aeppli, T. E. Mason and T. Armstrong, *Phys. Rev. Lett.* **70**, 3490 (1993).
- ¹⁹ L. V. Gasparov, P. Lemmens, M. Brinkmann, N. N. Kolesnikov, G. Güntherodt, *Phys. Rev. B* **55**, 1223 (1997).
- ²⁰ L. Capogna, B. Fauqué, Y. Sidis, C. Ulrich, P. Bourges, S. Pailhès, A. Ivanov, J. L. Tallon, B. Liang, C. T. Lin, A. I. Rykov and B. Keimer, *Phys. Rev. B* **75**, 060502(R) (2007).
- ²¹ G. Blumberg, M. Kang, M. V. Klein, K. Kadowaki and C. Kendziora, *Science* **278**, 1427 (1997).
- ²² S. Sugai, H. Suzuki, Y. Takayanagi, T. Hosokawa and N. Hayamizu, *Phys. Rev. B* **68**, 184504 (2003).
- ²³ C. Kendziora and A. Rosenberg, *Phys. Rev. B* **52**, R9867 (1995).
- ²⁴ T. Honma, P. H. Hor, H. H. Hsieh and M. Tanimoto, *Phys. Rev. B* **70**, 214517 (2004).
- ²⁵ T. Honma and P. H. Hor, *Supercond. Sci. Tech.* **19**, 907 (2006).
- ²⁶ T. Honma and P. H. Hor, *Phys. Rev. B* **75**, 012508 (2007).
- ²⁷ T. Nagano, Y. Tomioka, Y. Nakayama, K. Kishio and K. Kitazawa, *Phys. Rev. B* **48**, 9689 (1993).
- ²⁸ P. G. Radaelli, D. G. Hinks, A. W. Mitchell, B. A. Hunter, J. L. Wagner, B. Dabrowski, K. G. Vandervoort, H. K.

- Viswanathan and J. D. Jorgensen, *Phys. Rev. B* **49**, 4163 (1994).
- ²⁹ N. Kakinuma, Y. Ono and Y. Koike, *Phys. Rev. B* **59**, 1491 (1999).
- ³⁰ S. Komiya, H. D. Chen, S. C. Zhang and Y. Ando, *Phys. Rev. Lett.* **94**, 207004 (2005).
- ³¹ A. Yamamoto, W. Z. Hu and S. Tajima, *Phys. Rev. B* **63**, 024504 (2000).
- ³² J. A. Wilson and M. Farbod, *Supercond. Sci. Tech.* **13**, 307 (2000).
- ³³ Y. Ando, Y. Hanaki, S. Ono, T. Murayama, K. Segawa, N. Miyamoto, and S. Komiya, *Phys. Rev. B* **61**, R14956 (2000).
- ³⁴ Y. Okada and H. Ikuta, *Physica (Amsterdam)* **445-448C**, 84 (2006).
- ³⁵ Lin Shu-yuan, Lu Li, Zhang Dian-lin, H. M. Duan, William Kiehl and A. M. Hermann, *Phys. Rev. B* **47**, 8324 (1993).
- ³⁶ C. Martin, J. Hejtmanek, Ch. Simon, A. Maignan and B. Raveau, *Physica (Amsterdam)* **250C**, 235 (1995).
- ³⁷ J. L. Wagner, O. Chmaissem, J. D. Jorgensen, D. G. Hinks, P. G. Radaelli, B. A. Hunter and W. R. Jensen, *Physica (Amsterdam)* **277C**, 170 (1997).
- ³⁸ A. Ino, C. Kim, M. Nakamura, T. Yoshida, T. Mizokawa, A. Fujimori, Z. -X. Shen, T. Kakeshita, H. Eisaki and S. Uchida, *Phys. Rev. B* **65**, 094504 (2002).
- ³⁹ T. Yoshida, X. J. Zhou, K. Tanaka, W. L. Yang, Z. Hussain, Z. -X. Shen, A. Fujimori, S. Sahrakorpi, M. Lindroos, R. S. Markiewicz, A. Bansil, S. Komiya, Y. Ando, H. Eisaki, T. Kakeshita and S. Uchida, *Phys. Rev. B* **74**, 224510 (2006).
- ⁴⁰ T. Kondo, T. Takeuchi, U. Mizutani, T. Yokoya, S. Tsuda and S. Shin, *Phys. Rev. B* **72**, 024533 (2005).
- ⁴¹ M. Merz, N. Nücker, P. Schweiss, S. Schuppler, C. T. Chen, V. Chakarian, J. Freeland, Y. U. Idzerda, M. Kläser, G. Müller-Vogt and Th. Wolf, *Phys. Rev. Lett.* **80**, 5192 (1998).
- ⁴² H. Kotegawa, Y. Tokunaga, K. Ishida, G. -q. Zheng, Y. Kitaoka, H. Kito, A. Iyo, K. Tokiwa, T. Watanabe and H. Ihara, *Phys. Rev. B* **64**, 064515 (2001).
- ⁴³ N. E. Hussey, M. Abdel-Jawad, A. Carrington, A. P. Mackenzie and L. Balicas, *Nature* **425**, 814 (2003).
- ⁴⁴ J. R. Cooper, H. Minami, V. W. Wittorff, D. Babić and J. W. Loram, *Physica (Amsterdam)* **341-348C**, 855 (2000).
- ⁴⁵ A. Knizhnik, Y. Direktovich, G. M. Reisner, D. Goldschmidt, C. G. Kuper and E. Eckstein, *Physica (Amsterdam)* **321C**, 199 (1999).
- ⁴⁶ K. Hayashi, K. Matsuura, Y. Okajima, S. Tanda, N. Homma and K. Yamaya, *Czech. J. Phys.* **46** (S2), 1171 (1996).
- ⁴⁷ C. K. Subramaniam, C. V. N. Rao, A. B. Kaiser, H. J. Trodahl, A. Mawdsley, N. E. Flower and J. L. Tallon, *Supercond. Sci. Tech.* **7**, 30 (1994).
- ⁴⁸ J. W. Loram, K. A. Mirza, J. R. Cooper and J. L. Tallon, *J. Phys. Chem. Solids* **59**, 2091 (1998).
- ⁴⁹ C. K. Subramaniam, A. B. Kaiser, H. J. Trodahl, A. Mawdsley and R. G. Buckley, *Physica (Amsterdam)* **203C**, 98 (1992).
- ⁵⁰ M. Akoshima, T. Noji, Y. Ono and Y. Koike, *Phys. Rev. B* **57**, 7491 (1998).
- ⁵¹ J. B. Mandal, A. N. Das and B. Gosh, *J. Phys. Cond. Matter* **8**, 3047 (1996).
- ⁵² E. Kandyle, *Physica (Amsterdam)* **422C**, 102 (2005).
- ⁵³ Y. Cao, F. Y. Lin, Z. L. Du, F. Chen, Y. Y. Xue and C. W. Chu, *Physica (Amsterdam)* **282-287C**, 1243 (1997).
- ⁵⁴ A. Fukuoka, A. Tokiwa-Yamamoto, M. Itoh, R. Usami, S. Adachi and K. Tanabe, *Phys. Rev. B* **55**, 6612 (1997).
- ⁵⁵ J. L. Cohn, C. P. Popoviciu, Q. M. Lin and C. W. Chu, *Phys. Rev. B* **59**, 3823 (1999).
- ⁵⁶ T. Fujii, I. Terasaki, T. Watanabe and A. Matsuda, *Phys. Rev. B* **66**, 024507 (2002).
- ⁵⁷ C. K. Subramaniam, M. Paranthaman and A. B. Kaiser, *Phys. Rev. B* **51**, 1330 (1995).
- ⁵⁸ S. Mikusu, N. Urita, Y. Hashinaka, K. Tokiwa, A. Iyo, Y. Tanaka and T. Watanabe, *Physica (Amsterdam)* **442C**, 91 (2006).
- ⁵⁹ B. Wuyts, V. V. Moshchalkov, and Y. Bruynseraede, *Phys. Rev. B* **53**, 9418 (1996).
- ⁶⁰ T. Ito, K. Takenaka and S. Uchida, *Phys. Rev. Lett.* **70**, 3995 (1993).
- ⁶¹ M. Oda, K. Hoya, R. Kubota, C. Manabe, N. Momono, T. Nakano and M. Ido, *Physica (Amsterdam)* **281C**, 135 (1997).
- ⁶² K. Takenaka, K. Mizuhashi, H. Takagi and S. Uchida, *Phys. Rev. B* **50**, 6534 (1994).
- ⁶³ D. Babić, J. R. Cooper, J. W. Hodby and C. Changkang, *Phys. Rev. B* **60**, 698 (1999).
- ⁶⁴ Y. Ando, S. Komiya, K. Segawa, S. Ono and Y. Kurita, *Phys. Rev. Lett.* **93**, 267001 (2004).
- ⁶⁵ J. W. Loram, K. A. Mirza, J. R. Cooper and W. Y. Liang, *Phys. Rev. Lett.* **71**, 1740 (1993).
- ⁶⁶ V. V. Kabanov, J. Demsar, B. Podobnik and D. Mihailovic, *Phys. Rev. B* **59**, 1497 (1999).
- ⁶⁷ J. W. Loram, K. A. Mirza, J. R. Cooper and J. L. Tallon, *Physica (Amsterdam)* **282-287C**, 1405 (1997).
- ⁶⁸ J. R. Cooper and J. L. Tallon, *J. Phys. I (France)* **6**, 2237 (1996).
- ⁶⁹ J. W. Loram, J. L. Luo, J. R. Cooper, W. Y. Liang and J. L. Tallon, *Physica (Amsterdam)* **341-348C**, 831 (2000).
- ⁷⁰ M. Chiao, R. W. Hill, C. Lupien, L. Taillefer, P. Lambert, R. Gagnon and P. Fournier, *Phys. Rev. B* **62**, 3554 (2000).
- ⁷¹ J. Demsar, B. Podobnik, V. V. Kabanov, Th. Wolf and D. Mihailovic, *Phys. Rev. Lett.* **82**, 4918 (1999).
- ⁷² H. Ding, T. Yokoya, J. C. Campuzano, T. Takahashi, M. Randeria, M. R. Norman, T. Mochiku, K. Kadowaki and J. Giapintzakis, *Nature* **382**, 51 (1996).
- ⁷³ T. Sato, H. Matsui, S. Nishina, T. Takahashi, T. Fujii, T. Watanabe and A. Matsuda, *Phys. Rev. Lett.* **89**, 067005 (2002).
- ⁷⁴ R. M. Dipasupil, M. Oda, N. Momono and M. Ido, *J. Phys. Soc. Jpn.* **71**, 1535 (2002).
- ⁷⁵ D. H. Lu, D. L. Feng, N. P. Armitage, K. M. Shen, A. Damascelli, C. Kim, F. Ronning, Z. -X. Shen, D. A. Bonn, R. Liang, W. N. Hardy, A. I. Rykov and S. Tajima, *Phys. Rev. Lett.* **86**, 4370 (2001).
- ⁷⁶ A. Damascelli, D. Hussain and Z. X. Shen, *Rev. Mod. Phys.* **75**, 473 (2003).
- ⁷⁷ D. C. Peets, *New Journal of Physics* **9**, 28 (2007).
- ⁷⁸ J. Y. T. Wei, N. -C. Yeh, D. F. Garrigus and M. Strasik, *Phys. Rev. Lett.* **81**, 2542 (1998).
- ⁷⁹ Ch. Renner, B. Revaz, J. -Y. Genoud, K. Kadowaki and Ø. Fischer, *Phys. Rev. Lett.* **80**, 149 (1998).
- ⁸⁰ J. F. Zasadzinski, L. Ozyuzer, N. Miyakawa, K. E. Gray, D. G. Hinks and C. Kendziora, *Phys. Rev. Lett.* **87**, 067005 (2001).
- ⁸¹ L. Ozyuzer, J. F. Zasadzinski and N. Miyakawa, *Int. J. Mod. Phys. B* **131**, 3721 (1999).
- ⁸² M. Takigawa, A. P. Reyes, P. C. Hammel, J. D. Thomp-

- son, R. H. Heffner, Z. Fisk and K. C. Ott, Phys. Rev. B **43**, 247 (1991).
- ⁸³ A. Goto, H. Yasuoka and Y. Ueda, J. Phys. Soc. Jpn. **65**, 3043 (1996).
- ⁸⁴ K. Ishida, K. Yoshida, T. Mito, Y. Tokunaga, Y. Kitaoka, K. Asayama, A. Nakayama, J. Shimoyama and K. Kishio, Phys. Rev. B **58**, R5960 (1998).
- ⁸⁵ Y. Itoh, T. Machi, S. Adachi, A. Fukuoka, K. Tanabe and H. Yasuoka, J. Phys. Soc. Jpn. **67**, 312 (1998).
- ⁸⁶ B. Fauqué, Y. Sidis, V. Hinkov, S. Pailhès, C. T. Lin, X. Chaud and P. Bourges, Phys. Rev. Lett. **96**, 197001 (2006).
- ⁸⁷ Y. Kubo, Y. Shimakawa, T. Manako and H. Igarashi, Phys. Rev. B **43**, 7875 (1991).
- ⁸⁸ S. Pailhès, C. Ulrich, B. Fauqué, V. Hinkov, Y. Sidis, A. Ivanov, C. T. Lin, B. Keimer and P. Bourges, Phys. Rev. Lett. **96**, 257001 (2006).
- ⁸⁹ A. A. Maksimov, I. I. Tartakovskii, M. V. Klein and B. W. Veal, Phys. Rev. B **49**, 15385 (1994).
- ⁹⁰ K. C. Hewitt and J. C. Irwin, Phys. Rev. B **66**, 054516 (2002).
- ⁹¹ F. Venturini, M. Opel, R. Hackl, H. Berger, L. Forró and B. Revaz, J. Phys. Chem. Solids **63**, 2345 (2002).
- ⁹² S. Sugai and T. Hosokawa, Phys. Rev. Lett. **85**, 1112 (2000).
- ⁹³ M. Kang, G. Blumberg, M. V. Klein and N. N. Kolesnikov, Phys. Rev. Lett. **77**, 4434 (1996).
- ⁹⁴ M. Le Tacon, A. Sacuto, A. Georges, G. Kotliar, Y. Gallais, D. Coloson and A. Forget, Nature Physics **2**, 537 (2006).
- ⁹⁵ L. V. Gasparov, P. Lemmens, N. N. Kolesnikov, G. Güntherodt, Phys. Rev. B **58**, 11753 (1998).
- ⁹⁶ J. R. Cooper, B. Alavi, L. -W. Zhou, W. P. Beyermann and G. Grüner, Phys. Rev. B **35**, 8794 (1987).
- ⁹⁷ D. C. Johnston, J. P. Stokes, D. P. Goshorn and J. T. Lewandowski, Phys. Rev. B **36**, 4007 (1987).
- ⁹⁸ T. Nishikawa, J. Takeda and M. Sato, J. Phys. Soc. Jpn. **63**, 1441 (1994).
- ⁹⁹ J. -S. Zhou and J. B. Goodenough, Phys. Rev. B **51** 3104 (1995); **54**, 12488 (1996).
- ¹⁰⁰ Y. Park, B. H. Kim, J. S. Kim, D. C. Kim and B. Kim, J. Supercond. **18**, 743 (2005).
- ¹⁰¹ Y. Nakamura and S. Uchida, Phys. Rev. B **47**, 8369 (1993).
- ¹⁰² Z. A. Xu, N. P. Ong, T. Kakeshita, H. Eisaki and S. Uchida, Physica (Amsterdam) **341-348C**, 1711 (2000).
- ¹⁰³ J. -S. Zhou and J. B. Goodenough, Phys. Rev. B **56**, 6288 (1997).
- ¹⁰⁴ J. Ding Yu, Y. Inaguma, M. Itoh, M. Oguni and T. Kyômen, Phys. Rev. B **54**, 7455 (1996).
- ¹⁰⁵ M. Ambai, Y. Kobayashi, S. Iikubo and M. Sato, J. Phys. Soc. Jpn. **71**, 538 (2002).
- ¹⁰⁶ J. Takeda, T. Inukai and M. Sato, J. Phys. Soc. Jpn. **69**, 2917 (2000).
- ¹⁰⁷ F. Devaux, A. Manthiram and J. B. Goodenough, Phys. Rev. B **41**, 8723 (1990).
- ¹⁰⁸ A. J. Smits, W. J. Elion, J. M. van Ruitenbeek, L. J. de Jongh and W. A. Groen, Physica (Amsterdam) **199C**, 276 (1992).
- ¹⁰⁹ B. Lorenz, Z. G. Li, T. Honma and P. H. Hor, Phys. Rev. B **65**, 144522 (2002).
- ¹¹⁰ Y. Tokunaga, H. Kotegawa, K. Ishida, G. -q. Zheng, Y. Kitaoka, K. Tokiwa, A. Iyo and H. Ihara, J. of Low Temp. Phys. **117**, 473 (1999); Y. Tokunaga, K. Ishida, Y. Kitaoka, K. Asayama, K. Tokiwa, A. Iyo and H. Ihara, Phys. Rev. B **61**, 9707 (2000).
- ¹¹¹ J. L. Tallon, J. W. Loram, G. V. M. Williams, J. R. Cooper, J. R. Fisher, J. D. Johnson, M. P. Staines and C. Bernhard, Phys. Stat. Sol. (b) **215**, 531 (1999).
- ¹¹² D. Mihailovic and V. V. Kabanov, *Superconductivity in Complex Systems*, edited by K. A. Müller and A. Bussmann-Holder (Springer, Berlin/Heidelberg, 2005), vol. 14, p. 331.
- ¹¹³ S. Sanna, G. Allodi, G. Concas, A. D. Hillier and R. De Renzi, Phys. Rev. Lett. **93**, 207001 (2004); S. Sanna, G. Allodi and R. De Renzi, Solid State Commun. **126**, 85 (2003); S. Sanna, G. Allodi, G. Concas and R. De Renzi, J. Supercond. **18**, 769 (2005).
- ¹¹⁴ Ch. Niedermayer, C. Bernhard, T. Blasius, A. Golnik, A. Moodenbaugh and J. I. Budnick, Phys. Rev. Lett. **80**, 3843 (1998).
- ¹¹⁵ M. Matsuda, M. Fujita, K. Yamada, R. J. Birgeneau, Y. Endoh and G. Shirane, Phys. Rev. B **65**, 134515 (2002).
- ¹¹⁶ T. Nakano, M. Oda, C. Manabe, N. Momono, Y. Miura and M. Ido, Phys. Rev. B **49**, 16000 (1994).
- ¹¹⁷ R. Yoshizaki, N. Ishikawa, H. Sawada, E. Kita and A. Tasaki, Physica (Amsterdam) **166C**, 417 (1990).
- ¹¹⁸ D. C. Johnston, Phys. Rev. Lett. **62**, 957 (1989).
- ¹¹⁹ T. Nakano, N. Momono, T. Nagata, M. Oda and M. Ido, Phys. Rev. B **58**, 5831 (1998).
- ¹²⁰ T. Sato, T. Yokoya, Y. Naitoh, T. Takahashi, K. Yamada and Y. Endoh, Phys. Rev. Lett. **83**, 2254 (1999).
- ¹²¹ A. Ino, T. Mizokawa, K. Kobayashi, A. Fujimori, T. Sasagawa, T. Kimura, K. Kishio, K. Tamasaku, H. Eisaki and S. Uchida, Phys. Rev. Lett. **81**, 2124 (1998).
- ¹²² A. Ino, C. Kim, M. Nakamura, T. Yoshida, T. Mizokawa, Z. -X. Shen, A. Fujimori, T. Kakeshita, H. Eisaki and S. Uchida, Phys. Rev. B **62**, 4137 (2000).
- ¹²³ M. Hashimoto, T. Yoshida, K. Tanaka, A. Fujimori, M. Okusawa, S. Wakimoto, K. Yamada, T. Kakeshita, H. Eisaki and S. Uchida, Phys. Rev. B **75**, 140503(R) (2007).
- ¹²⁴ Y. Itoh, T. Machi, N. Koshizuka, M. Murakami, H. Yamagata and M. Matsumura, Phys. Rev. B **69**, 184503 (2004).
- ¹²⁵ P. Kusar, J. Demsar, D. Mihailovic and S. Sugai, Phys. Rev. B **72**, 014544 (2005).
- ¹²⁶ T. Nakano, N. Momono, M. Oda and M. Ido, J. Phys. Soc. Jpn. **67**, 2622 (1998).
- ¹²⁷ T. M. Rice, Phys. World **12**, 55 (1999).
- ¹²⁸ B. Watkins, H. Chashka, Y. Direktovich, A. Knizhnik, Y. Eckstein, Physica (Amsterdam) **450C**, 71 (2006).
- ¹²⁹ Risdiana, T. Adachi, N. Oki, S. Yairi, Y. Tanabe, K. Otori, Y. Koike, T. Suzuki, I. Watanabe, A. Koda and W. Higemoto, condmat-0707.3322v1; Physica C (Amsterdam) **460-462C**, 874 (2007).
- ¹³⁰ L. Krusin-Elbaum and T. Shibauchi, Int. J. Mod. Phys. B **21**, 3202 (2007).